Reduced graphene oxide decorated with SnO_2 nanoparticles as negative electrode for lithium ion capacitors

María Arnaiz [a, b], Cristina Botas [a], Daniel Carriazo [a, c], Roman Mysyk [a], Federico Mijangos [b], Teofilo Rojo [a, d], Jon Ajuria [a, *], Eider Goikolea [d, **]

[a] CIC energiGUNE, Albert Einstein 48, Technology Park of Araba, 01510, Miñano, Araba, Spain
[b] Chemical Engineering Department, University of the Basque Country UPV/EHU, P.O. Box 644, 48080, Bilbao, Spain
[c] Ikerbasque, Basque Foundation for Science, 48013, Bilbao, Spain
[d] Inorganic Chemistry Department, University of the Basque Country UPV/EHU, P.O. Box 644, 48080, Bilbao, Spain

ARTICLE INFO

ABSTRACT

The effort to increase the energy density of conventional electric double-layer capacitors (EDLCs) goes through the development of lithium-ion capacitors (LICs). Herein, we report a self-standing, binder-free composite as the battery-type negative electrode obtained by a low-cost and easily scalable method. Tin(IV) oxide nanoparticles (<10 nm) embedded in a reduced graphene oxide matrix (SnO_2-rGO) were prepared by an *in-situ* synthetic approach that involves the freeze/freeze-drying of a graphene oxide suspension in the presence of a tin precursor and its subsequent thermal reduction under argon atmosphere. Physicochemical and electrochemical characterization confirmed the optimum nanostructuration of the composite showing ultrafast response at high current densities. Its coupling with a highly porous olive pits waste-derived activated carbon (AC) as the capacitor-type positive electrode, enables the fabrication of a LIC with an excellent energy density output. The newly designed LIC is able to deliver 60 Wh kg^{-1} at 2.9 kW kg^{-1} ($t_{discharge} \approx 1$ min) and still 27 Wh kg^{-1} at 10.6 kW kg^{-1} ($t_{discharge} \approx 10$ s).

1. Introduction

In the last decades energy storage technologies have played a key role in the development of electronic devices which have nowadays become essential in our society. Currently, lithium-ion batteries (LIBs) dominate portable electronics market owing to their high energy density (~200 Wh kg^{-1}), slow energy delivery (hours) and low self-discharge characteristics. Instead, electrochemical capacitors (ECs) lead applications such as transportation-related regenerative braking energy (RBE) storage, start-stop systems in hybrid electric vehicles, small power tools and emergency backup power for the grid (where the required power density is very high, >10 kW kg^{-1}) [1–4]. Still, there are many applications, such as kinetic energy harvesting systems, which require a combination of both high energy and power densities. Thus, in order to bridge the gap between LIBs and ECs, lithium-ion electrochemical capacitors, commonly known as lithium-ion capacitors (LICs), were developed. LICs are meant to be used in all those applications that require high energy in charge/discharge times typically below *ca.* 2 min [5]. Briefly, in most of these systems a battery-type material replaces the negative electrode of a typical electrical double layer capacitor (EDLC). The former stores energy by means of faradic reactions taking place in the bulk of the material allowing for i) capacity increase due to the charge stored by faradic mechanism, which is much higher than that stored by non-faradic mechanism and ii) widening of the operating output voltage, since the potential of the negative electrode *vs.* lithium can be lowered [6]. The capacitor-type electrode stores charge by means of physical adsorption of ions at the electrode/electrolyte interface. Thus, the low-potential battery-type electrode allows the full hybrid cell to store a higher amount of charge and have higher cell voltage, with both features providing higher energy density. Meanwhile, the capacitor-type electrode stores and releases energy

* Corresponding author.
** Corresponding author.
E-mail addresses: jajuria@cicenergigune.com (J. Ajuria), eider.goikolea@ehu.eus (E. Goikolea).

rapidly providing high power density. Bringing both materials together enables the fabrication of a device with both high energy and high power densities combined with long cycle life [7].

The concept of asymmetric devices using a pseudofaradic or faradaic electrode was first coined at the end of 1990s [8]. Later, in 2001, a nonaqueous asymmetric electrochemical cell technology using nanostructured $Li_4Ti_5O_{12}$ (negative electrode) and activated carbon (AC) (positive electrode) was reported [9]. Since then, the battery-type electrode has been the major focus of research since it is widely accepted that carbonaceous materials are the best choice for the capacitive electrode owing to their high specific surface area (SSA) and relatively low cost [10]. On the contrary, within the large portfolio of battery-type materials, many materials with their own particular set of assets, such as $Li_4Ti_5O_{12}$ [11,12], hard carbons [13,14] and the well-known graphite [15,16] have been studied for LICs without discerning the best candidate amongst them. Despite this fact, graphite has been the most commonly used negative electrode in LICs owing to its low operational potential (~0.1 V *vs.* Li/Li$^+$), low-cost and good cycle life. However, the sluggishness of graphite electrodes is the main limiting factor for the power density of LICs, hence materials research in the last years has been focused on the development of new generation negative electrode materials with improved specific high-rate capacity than that of graphite [17—20]. In this context, Fuji et al. reported a tin-based amorphous oxide composite that was able to deliver twice the reversible capacity of graphite, which triggered research in this direction [21—24]. In fact, currently Sn and SnO_2 have become two of the most promising materials owing to their low active potential (<0.3 V *vs.* Li/Li$^+$) and high theoretical reversible specific capacities of 994 and 782 mAh g^{-1} respectively, making them superior to the vast majority of materials in terms of capacity [25]. Nevertheless, these kinds of composites suffer from a large volume expansion upon lithiation (up to 300%) and consequently, due to the mechanical stress, they lack of sufficient cycling stability [19]. In order to overcome this limitation, an approach consisting on the encapsulation of Sn-based particles within a reduced graphene oxide (rGO) environment was reported by our group [26]. Thereby, SnO_2 sub-micron particles were *in-situ* embedded within rGO layers, which acted as a support buffering the volume changes undergone by the tin composites and as a conductive additive [27]. Based on this approach, our group recently presented a fully graphene based LIC showing outstanding energy-to-power ratios based on the combination of SnO_2-rGO and thermally expanded and physically activated reduced graphene oxide (a-TEGO) [24]. However, the relatively large SnO_2 particles size, still suffered significant volume changes, which led to significant mechanical stress and decreased the overall electrode cycle life, which was especially evident at high current rates. In order to circumvent this limitation, we have developed a modified synthesis method for the SnO_2-rGO composite. By applying this synthetic procedure, first, it was possible to decrease the SnO_2 particle size below <10 nm, offering shorter paths for lithium ion diffusion and thus enhancing the rate capability of the negative electrode material [28]. Second, a more homogeneous particle distribution within the carbon matrix was achieved, mitigating the stress produced by the volume change and improving the long-term electrochemical performance [29]. Third, it was possible to increase the SnO_2 loading owing to the decrease in particles size.

Regarding the materials used for the capacitor-type electrode, high SSAcombined with a narrow pore size distribution (PSD) are the main requirements to maximize ion adsorption/desorption onto the material surface. Derived from different sources, activated carbons (ACs) show excellent features such as high SSA, good electrical conductivity, high capacitance values and high cycle life. In addition, they show moderate cost and large availability [30].

Driven by the environmental awareness, the use of natural waste precursors for the AC synthesis has been lately boosted. In our previous work, a-TEGO was used as the capacitor-type electrode since this type of graphene presents exceptional values regarding SSA and electronic conductivity [24]. Nevertheless, its low density penalizes volumetric values which are one of the major criterions towards implementation in real applications. Therefore, knowing that olive pits derived ACs show excellent capacitive behaviour both in gravimetric and volumetric terms [14], this carbonaceous material was selected as the capacitor-type material of the final device. So, herein, we report a LIC using self-standing, binder-free, high loading nano-SnO_2-rGO composite and high density olive pits derived AC as the negative and positive electrode materials respectively.

2. Experimental

2.1. Synthesis of rGO and SnO_2-rGO composites

Graphene oxide (GO) was synthesized by a previously reported modified Hummers' method [31]. To prepare the GO aerogel, 100 ml of the GO suspension (5.2 mg ml^{-1}) was freeze/freeze-dried and then thermally treated at 1 °C min^{-1} to 250 °C to avoid the thermal exfoliation of GO layers and at 2 °C min^{-1} to 650 °C for 1 h under argon atmosphere (100 ml min^{-1}) in order to obtain rGO samples. To prepare SnO_2-rGO composites, first $SnSO_4$ (Sigma Aldrich) was slowly added to the GO suspension (5.2 mg ml^{-1}) at different SnO_2:rGO ratios (50:50, 75:25 and 90:10 wt%). All of them were stirred during 30 min at room temperature to obtain a homogeneous mixture and then some drops of 1 M NH_3 were added to increase the pH up to 9 to induce the precipitation of $Sn(OH)_2$ onto GO layers. The same procedure as for rGO was followed to obtain the composites. Foams were pressed and cut to obtain the desired electrode geometry before thermal reduction. Aerogels with tin loadings of ca. 90 wt% were not able to be processed as self-standing electrodes due to their poor mechanical properties, thus, they were not further characterized. Hereafter, the selected samples will be denoted as SnO_2-rGO-50 and SnO_2-rGO-75.

2.2. Synthesis of the activated carbon (AC)

The synthesis of the AC from olive pits was performed following the method previously reported by Redondo et al. [32].

2.3. Physicochemical characterization

X-ray diffraction (XRD) patterns for *ex-situ* electrode samples were recorded in a Bruker D8 X-ray diffractometer; data was collected at 40 kV and 30 mA using CuKα radiation over a 2θ range between 20 and 70°. XRD patterns for *in-situ* electrode material were recorded in a Bruker D8 X-ray diffractometer; data was collected at 40 kV and 30 mA using CoKα radiation over a 2θ range between 27 and 47°. Raman spectra were recorded with a Renishaw spectrometer (Nanonics Multiview 2000) operating at an excitation wavelength of 532 nm. The spectra were acquired after 10 s of exposition time of the laser beam into the sample. Scanning Electron Microscopy (SEM) and Transmission Electron Microscopy (TEM) images were acquired with a field emission Quanta 200 FEG microscope and a Tecnai F20 microscope from FEI, respectively. To perform TEM measurements, all carbon samples were ground with acetone and the resulting sample dispersions of the powder carbon samples were transferred onto a holey carbon film fixed on a 3 mm copper grid (200 mesh). Thermogravimetric (TG) measurements (Netzsch-STA 449 F3 Jupiter®) were conducted from room temperature to 1000 °C at a heating rate of 10 °C min^{-1} in synthetic air.

Nitrogen adsorption-desorption isotherms were obtained at −195.8 °C using a Micromeritics ASAP 2020 instrument with relative pressure values (P/P$_0$) between 10^{-8} and 0.995. Before the analysis samples were outgassed for 24 h at 200 °C. SSA and PSD values were calculated by using the recently-developed 2D Non-Local Density Functional Theory (2D NLDFT) treatment to the nitrogen adsorption branch isotherm using the data reduction software SAIEUS.

2.4. Electrode fabrication, LIC assembly and electrochemical characterization

Self-standing SnO$_2$-rGO electrodes were fabricated with no need of additive, neither binder nor conductive carbon. Olive pits derived AC electrodes were prepared by mixing the AC with polytetrafluoroethylene (PTFE, 60 wt% dispersion in H$_2$O, Sigma Aldrich) as the binder in a mass ratio of 95:5. The AC slurry was worked out until plasticity, rolled to obtain a film and transferred into a vacuum oven and dried at 80 °C under constant vacuum for 12 h before 0.95 cm^2 circular electrodes were cut out. The thickness of the electrodes used to assemble the final LIC was around 70 μm, which correspond to 2.8 mg and 3.1 mg in weight for SnO$_2$-rGO and AC respectively. SnO$_2$-rGO electrodes were electrochemically characterized in CR2032 type half cells using Li metal both as the counter and the reference electrode. AC electrodes were electrochemically characterized in a three-electrode Swagelok® airtight system using Li metal as the reference electrode and commercial activated carbon YP-80F (Kuraray, Japan) as the counter electrode. Oversized (thicker) YP-80F electrodes were used as counter electrodes to ensure that their higher surface area kept up their potential within the electrolyte stability window. The final LIC was assembled in a three-electrode Swagelok® airtight system using Li metal as the reference electrode. All the electrochemical tests were conducted using 1 M LiPF$_6$ in ethylene carbonate (EC) and dimethyl carbonate (DMC) 1:1 (v/v) as the electrolyte (ca. 8.80 mS cm^{-1} at 20 °C) and a glass fiber membrane (Whatman GFB) as the separator, and were assembled inside a glove box under argon atmosphere. For comparison purposes, an EDLC using the same AC was assembled using 1.5 M tetraethylammonium tetrafluoroborate (NEt$_4$BF$_4$) in acetonitrile (57 mS cm^{-1}). The thickness and weight of the AC electrodes was around 75 μm and 3.5 mg respectively. The system was electrochemically characterized between 0 and 2.7 V. Cyclic voltammetry (CV) and galvanostatic (GA) charge/discharge measurements were recorded with a multichannel potentiostat (Biologic VMP3, France).

3. Results and discussion

3.1. Physicochemical characterization of materials

X-ray diffraction patterns of SnO$_2$-rGO-50 and SnO$_2$-rGO-75 are shown in Fig. 1a. The three main peaks at 26.7°, 34.2° and 51.9° assigned to the (110), (101) and (211) planes can be ascribed to the crystalline tetragonal rutile structure of SnO$_2$ (JCPDS card 41-1445). It is worth noticing that both diffraction patterns exhibit broad maxima, which is characteristic of nanosized compounds. The intensity of the diffraction maxima of the SnO$_2$-rGO-50 sample is lower due to its lower nanoparticles content. The characteristic diffraction peak corresponding to (002) planes from the rGO matrix is hidden by the broad (110) peak of the SnO$_2$ nanoparticles [26].

The amount of SnO$_2$ in each composite was quantified by means of thermogravimetric analysis (Fig. S1). TGA curves also show that in those samples containing SnO$_2$, rGO burns at lower temperature (450 °C) compared with the SnO$_2$-free sample, which occurs at ca. 620 °C. This difference should be ascribed to the catalytic effect of SnO$_2$ nanoparticles, which contribute with an additional amount of oxygen. Structural properties were also studied by Raman spectroscopy (Fig. 1b). Raman spectra of both SnO$_2$-rGO samples showed bands at 1350 and 1580 cm^{-1}, which correspond to the disordered (D) and graphitic (G) bands of carbon materials. The D band is generated by out of plane vibrations attributed to the presence of structural defects, whereas the G band is the result of in-plane vibrations of sp^2 bonded carbon atoms. As expected, the ratio between the I$_D$ and I$_G$ bands was very similar and slightly higher than one (I$_D$/I$_G$ = 1.1) in both cases. This value can be ascribed to the high porosity and the related large amount of defects of the graphene matrix [33]. Additionally, two peaks are observed at 450 and 610 cm^{-1}, corresponding to E$_g$ and A$_{1g}$ vibrations of the tin (IV) oxide [34].

Microstructural analysis carried out by different electron microscopy techniques clearly point out morphological differences between the original synthesis method where the suspension was mixed at 60 °C during 5 h [26] and the current modified synthesis route where the suspension was mixed at room temperature during 30 min. FE-SEM analysis reveals a clear evolution from sub-micron to nanosized SnO$_2$ particles. As it can be observed in Fig. 2a, sub-micron particles (approx. 250 nm in diameter) are deposited on rGO layers, while in Fig. 2b only tiny dots (in the range of <10 nm) are visible lying on rGO sheets. SnO$_2$-rGO samples were further studied by means of TEM. Fig. 2c and 2d show low resolution TEM micrographs for a single rGO layer decorated with SnO$_2$ nanoparticles of both SnO$_2$-rGO-50 and SnO$_2$-rGO-75 samples. The nanoparticle distribution along the rGO sheet is highly
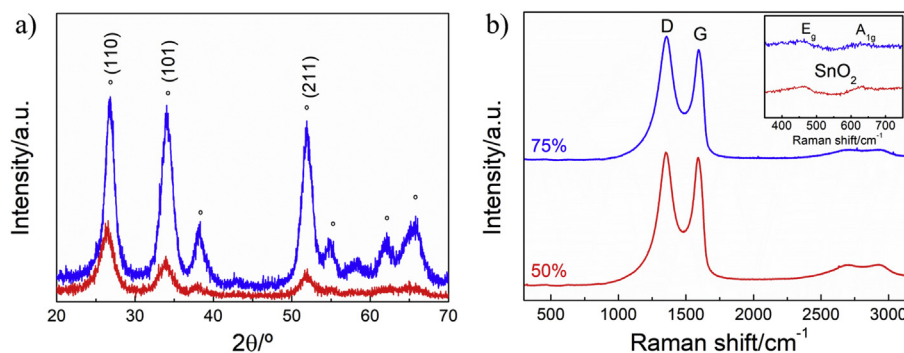
Fig. 1. a) XRD pattern using CuKα radiation for SnO$_2$-rGO-50 (red) and SnO$_2$-rGO-75 (blue) where (°) describes the peaks corresponding to the SnO$_2$ phase. b) Raman spectra of SnO$_2$-rGO-50 (red) and SnO$_2$-rGO-75 (blue). Inset: magnification for SnO$_2$ bands. (For interpretation of the references to colour in this figure legend, the reader is referred to the Web version of this article.)
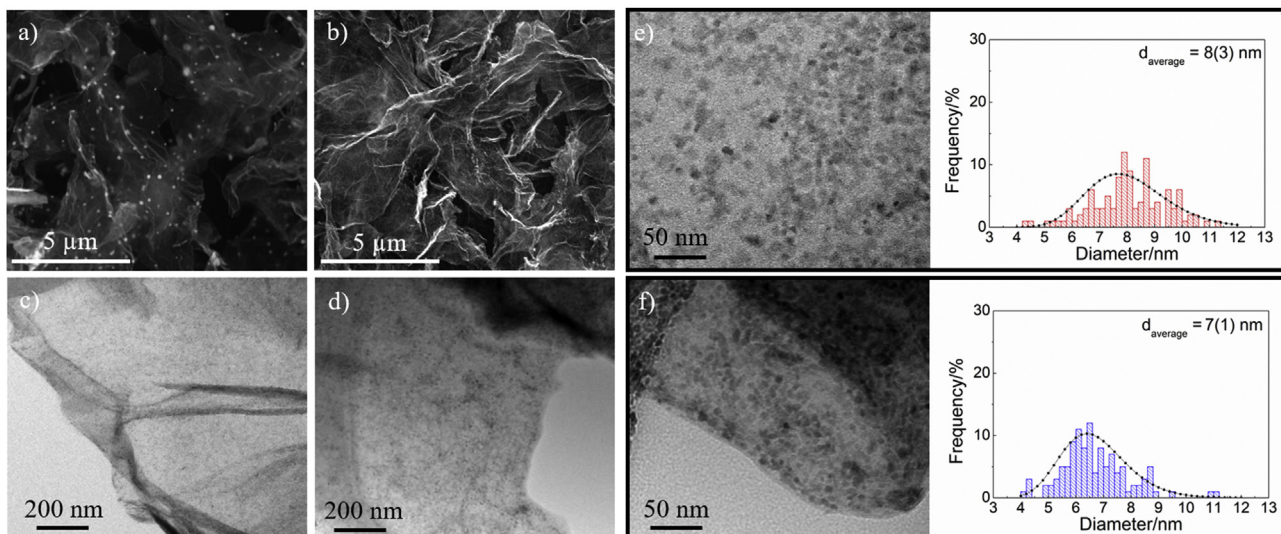
Fig. 2. a) SEM image of SnO$_2$-rGO sub-micron particles, b) SEM image of SnO$_2$-rGO-75 nanoparticles, c), e) TEM images of SnO$_2$-rGO-50, inset: histogram and d), f) TEM images of SnO$_2$-rGO-75 at different magnifications, inset: histogram.

homogeneous for both samples, although a higher population of nanoparticles can be inferred for the sample with the higher SnO$_2$ loading (SnO$_2$-rGO-75). This fact is confirmed by means of higher resolution micrographs shown in Fig. 2e and 2f where, furthermore, it is evidenced that nanoparticles have a mean particle size of 8 and 7 nm respectively, with almost no particles larger than 12 nm in diameter.

Textural properties of SnO$_2$-rGO composites were assessed by means of nitrogen adsorption-desorption isotherms (Fig. 3a). According to the IUPAC classification, these specific isotherms exhibit a type II profile associated to a nonporous or macroporous material. The SSA and the average pore size values calculated by 2D NLFT theory were 46 m^2 g^{-1} and 12 nm for SnO$_2$-rGO-50 and 101 m^2 g^{-1} and 14 nm for SnO$_2$-rGO-75. Thus, it is confirmed that the use of graphene as support provides an additional open structure which is favorable for electrolyte propagation towards pores and nanoparticles [35]. Furthermore, the high macroporosity of the graphene-based matrix might help to accommodate the SnO$_2$ volume changes and provide a more effective lithium ion diffusion path, contributing to increase the capacity as well as extending the cycling performance [36]. Fig. 3b shows the isotherm of the AC, which saturates rapidly at low relative pressure with no noticeable sign of hysteresis. According to the IUPAC classification, this specific isotherm exhibits a type I profile which is related to a microporous

material. A very high DFT-SSA of 2008 m^2 g^{-1} and an average pore size of 1.07 nm were calculated for the AC, very convenient to provide fast adsorption/desorption of ions.

3.2. Electrochemical characterization

3.2.1. SnO$_2$-rGO composite

Electrochemical characterization of SnO$_2$-rGO-50 and SnO$_2$-rGO-75 composites consisted of CVs registered between 0.005 and 3 V at 0.1 mV s^{-1} sweep rate and, GA charge/discharge experiments at different current densities between 0.05 and 5.0 A g^{-1} in the potential range of 0.005-2.0 V vs. Li/Li$^+$ were carried out. In Fig. 4 the first two cycles of both CVs and GA charge/discharge profiles for each composite are shown. On the one hand, voltammograms shown in Fig. 4a reveal two main peaks at 0.88 and 0.10 V within the first discharge step (cathodic sweep) which are associated to the irreversible conversion reaction of SnO$_2$ into metallic Sn (eq. (1)) and to the SEI (Solid Electrolyte Interphase) formation. Peaks below 0.1 V are ascribed to the alloying process of Li$_x$Sn (eq. (2)). This correlates well with the 1st GA discharge profile shown in Fig. 4b, where a discharge plateau at around 1 V and a decreasing sloping profile region between 0.8 V and 0.3 V is observed for the SEI formation and conversion reaction respectively. On the other hand, in the 1st charge step (anodic sweep), two main peaks
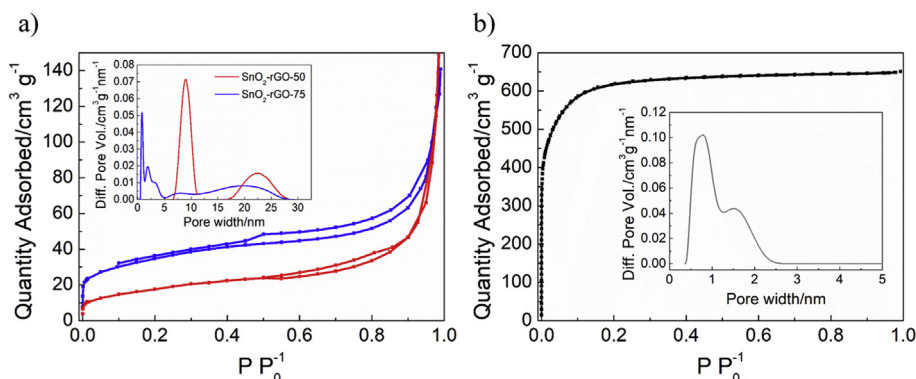

Fig. 3. Isotherms of a) SnO$_2$-rGO-50 and -75 composites and b) Olive pits derived AC, inset: PSD.
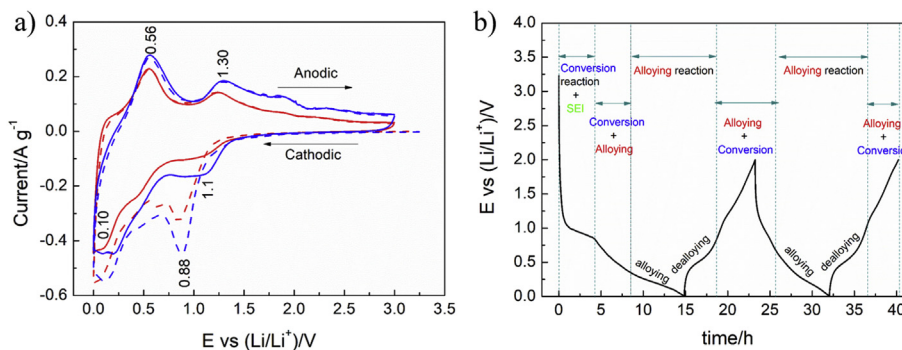
Fig. 4. a) Cyclic voltammetry 1st (solid line) and 2nd (dash line) cycles of SnO$_2$-rGO-50 (red) and SnO$_2$-rGO-75 (blue) composites. b) 1st and 2nd charge/discharge profiles for SnO$_2$-rGO-75 composite. (For interpretation of the references to colour in this figure legend, the reader is referred to the Web version of this article.)

appeared at 0.56 and 1.30 V. The peak observed at 0.56 V is assigned to the dealloying from Li$_x$Sn, meanwhile at 1.30 V the reversible conversion of Sn into SnO$_2$ occurs [37–40]. The same potentials of the corresponding transformations are evident from the GA profiles (Fig. 4b). It is also concluded that the composite with the highest tin loading (SnO$_2$-rGO-75), should provide higher specific capacity values due to the higher area of the peaks. Thus, it is selected as the battery-type negative electrode for the final LIC.

$$SnO_2 + 4\,Li^+ + 4\,e^- \Rightarrow 2\,Li_2O + Sn \tag{1}$$

$$Sn + x\,Li^+ + x\,e^- \Leftrightarrow Li_xSn (0 \leq x \leq 4.4) \tag{2}$$
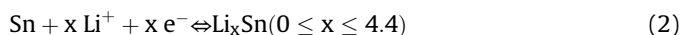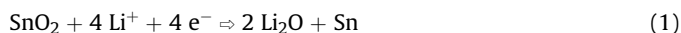
Furthermore, *in-situ* recorded XRD allow us to validate the reaction mechanisms by following the structural changes upon cycling. Fig. 5 shows the evolution of the *in-situ* XRD patterns registered for the SnO$_2$-rGO-75 during the first cycle between 2.0 V and 0.005 V *vs.* Li/Li$^+$ at C/40 ≈ ca. 0.02 A g^{-1}. First, the XRD pattern at open-circuit cell potential (OCV) shows two peaks at 35.8° and 37.5° assigned to the (101) and (211) planes, which correspond to the crystalline rutile tetragonal structure of SnO$_2$ (JCPDS card 41-1445). The additional peaks at 28.6°, 29.9°, 40.6° and 42.1° come from the stainless steel of the in-house made electrochemical cell. The SEI formation occurs during the first irreversible discharge above *ca.* 1.0 V *vs.* Li/Li$^+$. The XRD patterns recorded at those

potential values (in green in Fig. 5) show that the conversion reaction of SnO$_2$ into metallic Sn occurs in parallel to the growth of the SEI *(eq. I)*. Thus, the intensity of the diffraction maxima of the SnO$_2$ phase decreases until their complete disappearance and at 35.8° and 37.4° the peaks corresponding to the tetragonal structure of metallic tin (JCPDS card 04-0673) start appearing and becoming sharper for the lower potentials. At 0.6 V the alloying reaction starts and the peaks corresponding to metallic Sn are less intense *(eq. II)*. Both the alloying reaction (0.6-0.005 V, in red in Fig. 5) and the reverse dealloying reaction (0.005-0.9 V, in light red in Fig. 5) are not associated with any diffraction peak. Likely, this comes from the amorphous nature of the alloy and/or the small particle size. Above 0.9 V the peaks corresponding to metallic Sn are evident and maintained during charging and discharging until the second alloying reaction starts again at 0.6 V.

Due to the high content of SnO$_2$ within the composites, the electrodes have higher mass loadings (~2 mg) compared to those previously reported (~1 mg) [26]. Therefore, Fig. 6 also includes areal capacity values in addition to specific capacity values, to allow a fair comparison with the already reported values [26]. During the rate capability test, where the capacity evolution *vs.* the current density is analyzed, 20 cycles were necessary to stabilize the alloying reaction and then higher current densities were applied. As it can be observed in Fig. 6a, high capacity values of 600 mAh g^{-1} and 450 mAh g^{-1} were obtained at lower current densities (i.e. 0.1
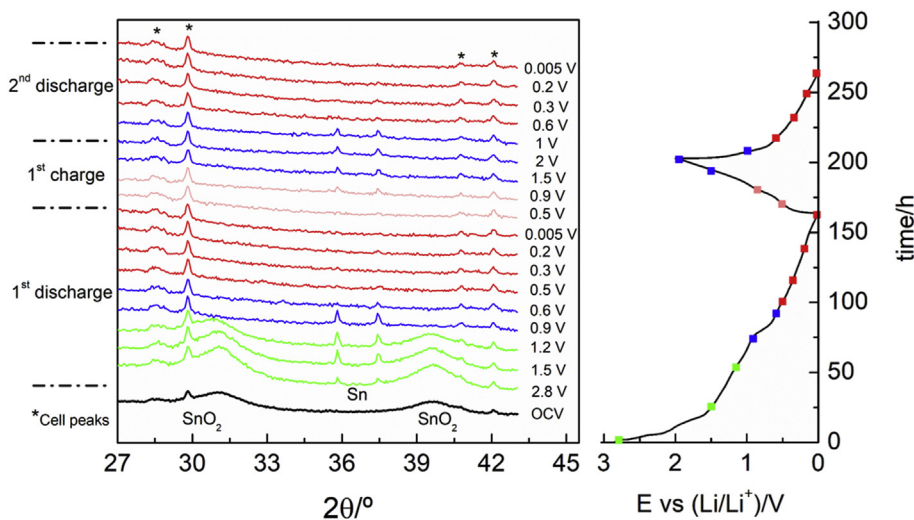
Fig. 5. In situ XRD patterns using CuKα radiation for SnO$_2$-rGO-75 and its electrochemical behavior.
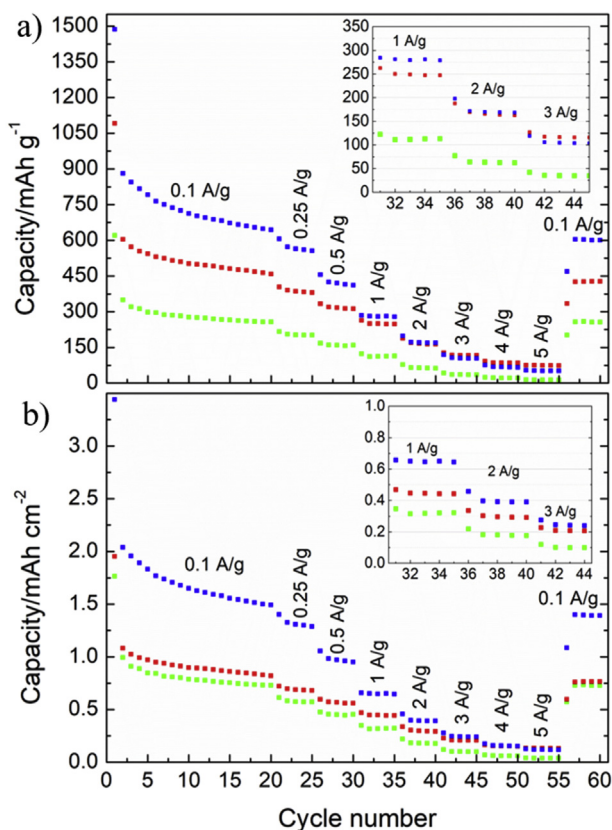
Fig. 6. Rate capability of SnO$_2$-rGO-75 (blue), SnO$_2$-rGO-50 (red) and rGO (green). a) Specific gravimetric capacity values b) Specific areal capacity values. Inset: magnification for high current densities. (For interpretation of the references to colour in this figure legend, the reader is referred to the Web version of this article.)

A g^{-1}) for SnO$_2$-rGO-75 and SnO$_2$-rGO-50, respectively. In order to quantify the contribution of rGO to the overall capacity, a blank sample of only rGO was also characterized showing a capacity value of 258 mAh g^{-1}. At higher current densities of 1, 2 and 3 A g^{-1} (inset Fig. 6a and 6b), specific capacity values of 250, 165 and 115 mAh g^{-1} were obtained for SnO$_2$-rGO-50 and 280, 175 and 110 mAh g^{-1} for SnO$_2$-rGO-75, evidencing the slightly superior performance of the latter electrode. These good results at high current densities are ascribed to the importance of having an excellent conductive matrix made of rGO [41]. In terms of areal capacity, see Fig. 6b, it is also confirmed that the higher SnO$_2$ loading provides higher areal capacity values throughout the whole studied current density range.

The capacity difference between SnO$_2$-rGO-50 and rGO is larger in gravimetric terms than in terms of areal capacity values due to the different weight of the electrodes. Also, these results confirm the expected superior capacity performance achieved by nanosized composites as compared to the previously reported sub-micron composite. As at high currents densities (i.e. 1 A g^{-1}) lower capacity values (0.45 mAh cm^{-2} *vs.* 0.63 mAh cm^{-2}) were achieved (Fig. S2).

3.2.2. Olive pits derived AC

GA charge/discharge measurements for the olive pits derived AC were previously reported by our group [14]. In Fig. S3 volumetric capacitance values of previously used a-TEGO and those calculated for the olive pits derived AC are compared. It should be highlighted that owing to the higher apparent density of the AC electrode (0.5 g cm^{-3}) with respect to that of the a-TEGO (0.3 g cm^{-3}), volumetric capacitance values are nearly doubled in the whole range of current densities if olive pits derived AC is used instead of a-TEGO.

3.3. Li-ion capacitor assembly and characterization

As stated before, SnO$_2$-rGO-75 nanocomposite was selected as the negative electrode material for the LIC since it outperforms its SnO$_2$-rGO-50 counterpart in terms of specific capacity. For the positive electrode, previously reported olive pits derived AC was selected, and a full LIC cell was assembled with those two electrodes in a T-shaped Swagelok® cell using 1 M LiPF$_6$ (EC:DMC) electrolyte. A key factor for the successful assembly of a LIC is an accurate mass balance of the electrodes in order to maximize the performance of the system. As the charge stored in both electrodes must be equal (Q$_+$ = Q$_-$) and is directly proportional to the specific capacitance and the operational output potential difference (Q α C · V), the mass ratio of the electrodes must be balanced to get the maximum capacity output in both materials [42]. As it can be observed in Fig. S4, the capacity of both materials diverges along the applied current density values and, thus, it is not possible to define a suitable mass balance for the whole range. Since LICs are designed to be used in low discharge time applications, typically below 2 min, a mass ratio of 1:1 was selected owing to the similar capacity values of both materials at high current densities (Fig. S4).

The GA charge/discharge characterization of the LIC was performed between 1.5 and 4.2 V *vs.* Li/Li$^+$ at current densities between 0.05 and 5 A g^{-1}. In Fig. 7, the profiles of both electrodes and the LIC are shown at 0.1, 1 and 3 A g^{-1}. At low current densities, i.e. 0.1 A g^{-1}, within a discharge time of 26 min, the positive electrode swings from 2.2 to 4.2 V *vs.* Li/Li$^+$ showing an ideal symmetric profile indicative of the capacitive storage mechanism, while the negative electrode swings in a potential window from 0.8 to 0.1 V. A
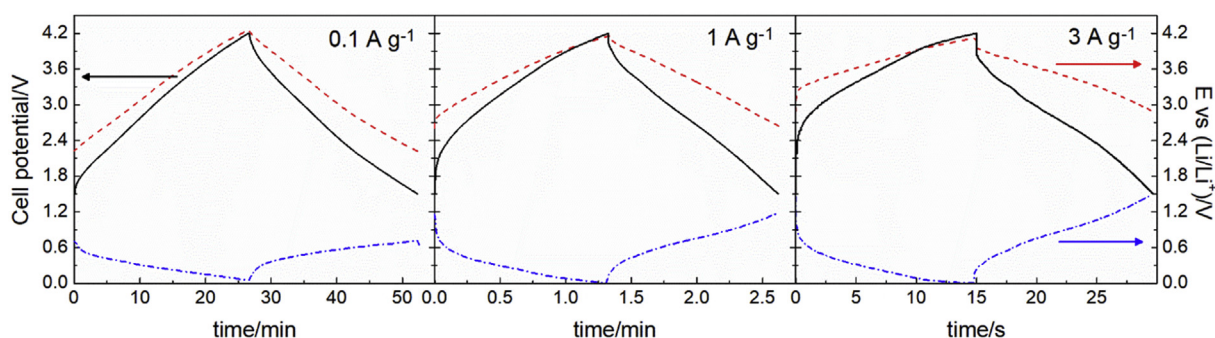
Fig. 7. GA charge/discharge profiles of positive (AC in dash red line) and negative (SnO$_2$-rGO-75 in dash-dot blue line) electrodes and full cell (LIC in black). (For interpretation of the references to colour in this figure legend, the reader is referred to the Web version of this article.)

10-fold increase in the applied current density, from $0.1\,A\,g^{-1}$ to $1\,A\,g^{-1}$, decreases the discharge time to 29 s, a discharge time restricted to supercapacitors, unattainable for batteries. Although potential profiles are slightly distorted from ideality, the increase in the ohmic resistance of the overall system is negligible and thus, the LIC charge/discharge profile is still determined by a capacitive charge store mechanism. A further 30-fold increase in the current, from $0.1\,A\,g^{-1}$ to $3\,A\,g^{-1}$, reduces the discharge time down to 9 s. At this extremely challenging discharge time, the positive electrode still manages to work in a secure potential window, without going beyond the electrolytic decomposition potential while the negative electrode is able to work in a potential window of 0.005–1.5 V *vs.* Li/Li$^+$, using its maximum capacity. Thus, it is confirmed that the 1:1 mass balance is ideally suitable for extremely rapid discharge times as for hybrid supercapacitors being the charge storage capacities of both electrode materials well balanced.

Fig. 8a shows a comparison among the energy-to-power density ratios of the developed LIC with our already reported graphene-based LIC (LIC$_{a-TEGO}$) [24], other state-of-the-art systems [14,15,24,42–49] and the EDLC counterpart (AC/AC). The reported results show that at medium-high power density values (about $5400\,W\,kg^{-1}$ and $t_{discharge} < 1\,min$), our newly developed LIC is able to deliver $44\,Wh\,kg^{-1}$ while the energy density of LIC$_{a-TEGO}$ was $34\,Wh\,kg^{-1}$. Moreover, the replacement of graphene by AC, *i.e.* the substitution of the low-packing density material, would make the response of the new LIC superior in the whole studied power

density region in terms of total mass of the device [50]. Furthermore, the energy and power density values obtained for this LIC are comparable with other works found in the literature. Additionally, the LIC is able to store and deliver between 5- and 3-times more gravimetric and volumetric (Fig. S5a) energy density than its EDLC counterpart.

Following the aforementioned criteria for a fair comparison with previously reported results, Fig. 8b shows the areal energy-to-power comparison of the current LIC and LIC$_{a-TEGO}$. It is evident that the newly developed nanostructured SnO$_2$-rGO electrode has a clear impact over its sub-micron sizedcounterpart, allowing the new LIC to double the areal energy density with respect to LIC$_{a-TEGO}$ at the low power region and increasing it by a factor of 6 at high power density values. Still, the great challenge of a LIC is to keep the cycle life as close as possible to that of an EDLC. Thus, a stability test was run at $3\,A\,g^{-1}$ ($t_{discharge} = 15\,s$) showing a promising capacitance retention of 65% after 5000 cycles and a 55% retention after 10000 cycles (Fig. S5b). The acceptable number of cycles accomplished for this LIC is ascribed to the nanosize of SnO$_2$ particles decorating the rGO matrix, which significantly reduces the mechanical stress of the negative electrode, extending the cycle life of the overall device.

4. Conclusions

Based on our previous research on SnO$_2$-rGO composites, in this work we have modified the synthesis route to boost the electrochemical performance of the more sluggish negative electrode with the intended use in LICs. Nanosized SnO$_2$ particles (<10 nm) were obtained instead of the previously reported sub-micron SnO$_2$ particles ($\approx 250\,nm$), which allowed for higher SnO$_2$ loading -up to 75 wt%- onto graphene layers without increasing mechanical stress. The high SnO$_2$ content translates into a remarkable electrochemical performance, especially at medium and high current densities, a highly appealing feature for ultrafast LICs. The combination of a SnO$_2$-rGO composite with recycled, therefore low-cost, olive pits derived AC enables targeting high energy density LICs with excellent gravimetric and volumetric characteristics. Altogether, this coupling gives the opportunity to assemble an encouraging hybrid device which stores/delivers high energy densities at high power densities. In fact, at low power densities, a 5-fold -gravimetric- and a 6-fold -volumetric- increase was achieved in terms of energy density. At the high power region the energy density was still between double and treble that of the EDLC using the same porous carbon. Moreover, comparison with the previously reported sub-micron SnO$_2$-rGO and a-TEGO based LIC at the high power density region, where hybrid supercapacitors should work better, demonstrates that the newly developed LIC based on nano SnO$_2$-rGO and olive pits derived AC provides a substantial gain in areal energy density. In addition, the system presents a highly promising 55% capacitance retention after 10000 cycles run at a discharge time of 15 s.
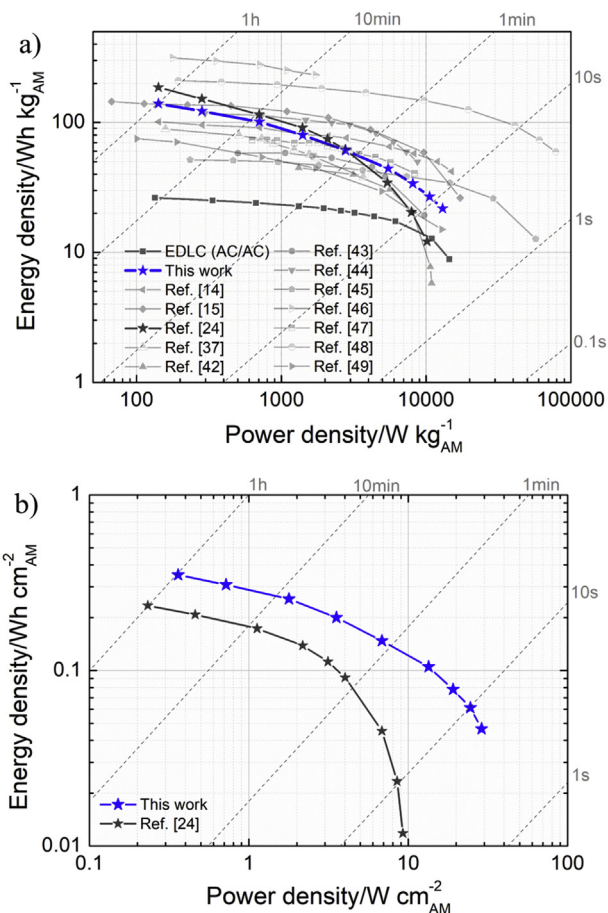
Fig. 8. a) Gravimetric and b) Volumetric Ragone plots comparing the olive pits derived EDLC and the new reported LIC and c) Areal Ragone plot for comparison with the previous work (Ref. [24]). d) Stability of the newly developed LIC at $3\,A\,g^{-1}$ ($t_{discharge} = 15\,s$).

Appendix A. Supplementary data

Supplementary data related to this article can be found at https://doi.org/10.1016/j.electacta.2018.07.189.

References

[1] Li-ion Portable Battery Market - Global Industry Analysis and Forecast | 2025, http://www.transparencymarketresearch.com/li-ion-portable-battery-market.html (accessed September 9, 2017).

[2] J.R. Miller, Engineering electrochemical capacitor applications, J. Power Sources 326 (2016) 726–735, https://doi.org/10.1016/j.jpowsour.2016.04.020.

[3] J.R. Miller, A.F. Burke, Electrochemical capacitors: challenges and opportunities for real-world applications, Electrochem. Soc. Interface 17 (1) (2008) 53. https://www.electrochem.org/dl/interface/spr/spr08/spr08_p53-57.pdf. (Accessed 6 November 2017).

[4] Applications - Yunasko is the developer and licensor of high power ultracapacitors, http://yunasko.com/en/applications (accessed September 20, 2017).

[5] Lithium Ion Capacitor Products | JSR Micro, Inc., https://www.jsrmicro.com/emerging-technologies/lithium-ion-capacitor/lithium-ion-capacitor-products (accessed June 22, 2018).

[6] P. Simon, Y. Gogotsi, B. Dunn, Where do batteries end and supercapacitors begin? Science 343 (2014) 1210–1211, https://doi.org/10.1126/science.1249625.

[7] K. Naoi, 'Nanohybrid capacitor': the next generation electrochemical capacitors, Fuel Cells 10 (2010) 825–833, https://doi.org/10.1002/fuce.201000041.

[8] S. Razoumov, A. Klementov, S. Litvinenko, A. Beliakov, Asymmetric electrochemical capacitor and method of making, US Patent 6222723B1, 2001.

[9] G.G. Amatucci, F. Badway, A.D. Pasquier, T. Zheng, An asymmetric hybrid nonaqueous energy storage cell, J. Electrochem. Soc. 148 (2001) A930–A939, https://doi.org/10.1149/1.1383553.

[10] P.L. Taberna, P. Simon, J.F. Fauvarque, Electrochemical characteristics and impedance spectroscopy studies of carbon-carbon supercapacitors, J. Electrochem. Soc. 150 (2003) A292–A300, https://doi.org/10.1149/1.1543948.

[11] H.-G. Jung, N. Venugopal, B. Scrosati, Y.-K. Sun, A high energy and power density hybrid supercapacitor based on an advanced carbon-coated $Li_4Ti_5O_{12}$ electrode, J. Power Sources 221 (2013) 266–271, https://doi.org/10.1016/j.jpowsour.2012.08.039.

[12] K. Naoi, S. Ishimoto, Y. Isobe, S. Aoyagi, High-rate nano-crystalline $Li_4Ti_5O_{12}$ attached on carbon nano-fibers for hybrid supercapacitors, J. Power Sources 195 (2010) 6250–6254, https://doi.org/10.1016/j.jpowsour.2009.12.104.

[13] W.J. Cao, J.P. Zheng, Li-ion capacitors with carbon cathode and hard carbon/stabilized lithium metal powder anode electrodes, J. Power Sources 213 (2012) 180–185, https://doi.org/10.1016/j.jpowsour.2012.04.033.

[14] J. Ajuria, E. Redondo, M. Arnaiz, R. Mysyk, T. Rojo, E. Goikolea, Lithium and sodium ion capacitors with high energy and power densities based on carbons from recycled olive pits, J. Power Sources 359 (2017) 17–26, https://doi.org/10.1016/j.jpowsour.2017.04.107.

[15] V. Khomenko, E. Raymundo-Piñero, F. Béguin, High-energy density graphite/AC capacitor in organic electrolyte, J. Power Sources 177 (2008) 643–651, https://doi.org/10.1016/j.jpowsour.2007.11.101.

[16] M. Yuan, W. Liu, Y. Zhu, Y. Xu, Electrochemical performance of pre-lithiated graphite as negative electrode in lithium-ion capacitors, Russ. J. Electrochem. 50 (2014) 1050–1057, https://doi.org/10.1134/S1023193514020086.

[17] B. Scrosati, Recent advances in lithium ion battery materials, Electrochim. Acta 45 (2000) 2461–2466, https://doi.org/10.1016/S0013-4686(00)00333-9.

[18] S. Goriparti, E. Miele, F. De Angelis, E. Di Fabrizio, R. Proietti Zaccaria, C. Capiglia, Review on recent progress of nanostructured anode materials for Li-ion batteries, J. Power Sources 257 (2014) 421–443, https://doi.org/10.1016/j.jpowsour.2013.11.103.

[19] N. Nitta, F. Wu, J.T. Lee, G. Yushin, Li-ion battery materials: present and future, Mater. Today 18 (2015) 252–264, https://doi.org/10.1016/j.mattod.2014.10.040.

[20] V. Aravindan, Y.-S. Lee, S. Madhavi, Research progress on negative electrodes for practical Li-Ion batteries: beyond carbonaceous anodes, Adv. Energy Mater. 5 (2015), https://doi.org/10.1002/aenm.201402225.

[21] L. Yue, C. Xue, B. Huang, N. Xu, R. Guan, Q. Zhang, W. Zhang, High performance hollow carbon@SnO_2@graphene composite based on internal-external double protection strategy for lithium ion battery, Electrochim. Acta 220 (2016) 222–230, https://doi.org/10.1016/j.electacta.2016.10.110.

[22] M.V. Reddy, T.T. Linh, D.T. Hien, B.V.R. Chowdari, SnO_2 based materials and their energy storage studies, ACS Sustain. Chem. Eng. 4 (2016) 6268–6276, https://doi.org/10.1021/acssuschemeng.6b00445.

[23] F. Sun, J. Gao, Y. Zhu, X. Pi, L. Wang, X. Liu, Y. Qin, A high performance lithium ion capacitor achieved by the integration of a Sn-C anode and a biomass-derived microporous activated carbon cathode, Sci. Rep. 7 (2017), https://doi.org/10.1038/srep40990 srep40990.

[24] J. Ajuria, M. Arnaiz, C. Botas, D. Carriazo, R. Mysyk, T. Rojo, A.V. Talyzin, E. Goikolea, Graphene-based lithium ion capacitor with high gravimetric energy and power densities, J. Power Sources 363 (2017) 422–427, https://doi.org/10.1016/j.jpowsour.2017.07.096.

[25] X.-T. Chen, K.-X. Wang, Y.-B. Zhai, H.-J. Zhang, X.-Y. Wu, X. Wei, J.-S. Chen, A facile one-pot reduction method for the preparation of a SnO/SnO_2/GNS composite for high performance lithium ion batteries, Dalton Trans. 43 (2014) 3137–3143, https://doi.org/10.1039/C3DT52661E.

[26] C. Botas, D. Carriazo, G. Singh, T. Rojo, Sn– and SnO_2–graphene flexible foams suitable as binder-free anodes for lithium ion batteries, J. Mater. Chem. A. 3 (2015) 13402–13410, https://doi.org/10.1039/C5TA03265B.

[27] Z.-S. Wu, G. Zhou, L.-C. Yin, W. Ren, F. Li, H.-M. Cheng, Graphene/metal oxide composite electrode materials for energy storage, Nano Energy 1 (2012) 107–131, https://doi.org/10.1016/j.nanoen.2011.11.001.

[28] Y. Wang, H. Li, P. He, E. Hosono, H. Zhou, Nano active materials for lithium -ion batteries, Nanoscale 2 (2010) 1294–1305, https://doi.org/10.1039/C0NR00068J.

[29] Y. Xu, Q. Liu, Y. Zhu, Y. Liu, A. Langrock, M.R. Zachariah, C. Wang, Uniform Nano-Sn/C composite anodes for lithium ion batteries, Nano Lett. 13 (2013) 470–474, https://doi.org/10.1021/nl303823k.

[30] J. Wang, P. Nie, B. Ding, S. Dong, X. Hao, H. Dou, X. Zhang, Biomass derived carbon for energy storage devices, J. Mater. Chem. A. 5 (2017) 2411–2428, https://doi.org/10.1039/C6TA08742F.

[31] C. Botas, P. Álvarez, C. Blanco, R. Santamaría, M. Granda, P. Ares, F. Rodríguez-Reinoso, R. Menéndez, The effect of the parent graphite on the structure of graphene oxide, Carbon 50 (2012) 275–282, https://doi.org/10.1016/j.carbon.2011.08.045.

[32] E. Redondo, J. Carretero-González, E. Goikolea, J. Ségalini, R. Mysyk, Effect of pore texture on performance of activated carbon supercapacitor electrodes derived from olive pits, Electrochim. Acta 160 (2015) 178–184, https://doi.org/10.1016/j.electacta.2015.02.006.

[33] J. Shan, Y. Liu, P. Liu, Y. Huang, Y. Su, D. Wu, X. Feng, Nitrogen-doped carbon-encapsulated SnO_2 –SnS/graphene sheets with improved anodic performance in lithium ion batteries, J. Mater. Chem. A. 3 (2015) 24148–24154, https://doi.org/10.1039/C5TA06617D.

[34] J. Cheng, H. Xin, H. Zheng, B. Wang, One-pot synthesis of carbon coated-SnO_2/graphene-sheet nanocomposite with highly reversible lithium storage capability, J. Power Sources 232 (2013) 152–158, https://doi.org/10.1016/j.jpowsour.2013.01.025.

[35] Y. Deng, C. Fang, G. Chen, The developments of SnO_2/graphene nano-composites as anode materials for high performance lithium ion batteries: a review, J. Power Sources 304 (2016) 81–101, https://doi.org/10.1016/j.jpowsour.2015.11.017.

[36] M. Zhang, Z. Sun, T. Zhang, D. Sui, Y. Ma, Y. Chen, Excellent cycling stability with high SnO_2 loading on a three-dimensional graphene network for lithium ion batteries, Carbon 102 (2016) 32–38, https://doi.org/10.1016/j.carbon.2016.02.032.

[37] C.-L. Hsieh, D.-S. Tsai, W.-W. Chiang, Y.-H. Liu, A composite electrode of tin dioxide and carbon nanotubes and its role as negative electrode in lithium ion hybrid capacitor, Electrochim. Acta 209 (2016) 332–340, https://doi.org/10.1016/j.electacta.2016.05.090.

[38] J. Sun, L. Xiao, S. Jiang, G. Li, Y. Huang, J. Geng, Fluorine-doped SnO_2@Graphene Porous Composite for High Capacity Lithium-ion Batteries, 2015, https://doi.org/10.1021/acs.chemmater.5b00885.

[39] X. Zhou, L.-J. Wan, Y.-G. Guo, Binding SnO_2 nanocrystals in nitrogen-doped graphene sheets as anode materials for lithium-ion batteries, Adv. Mater. 25 (2013) 2152–2157, https://doi.org/10.1002/adma.201300071.

[40] L. Noerochim, J.-Z. Wang, S.-L. Chou, H.-J. Li, H.-K. Liu, SnO_2-coated multiwall carbon nanotube composite anode materials for rechargeable lithium-ion batteries, Electrochim. Acta 56 (2010) 314–320, https://doi.org/10.1016/j.electacta.2010.08.078.

[41] A. González, E. Goikolea, J.A. Barrena, R. Mysyk, Review on supercapacitors: technologies and materials, Renew. Sustain. Energy Rev. 58 (2016) 1189–1206, https://doi.org/10.1016/j.rser.2015.12.249.

[42] S. Dsoke, B. Fuchs, E. Gucciardi, M. Wohlfahrt-Mehrens, The importance of the electrode mass ratio in a Li-ion capacitor based on activated carbon and $Li_4Ti_5O_{12}$, J. Power Sources 282 (2015) 385–393, https://doi.org/10.1016/j.jpowsour.2015.02.079.

[43] B. Babu, P.G. Lashmi, M.M. Shaijumon, Li-ion capacitor based on activated rice husk derived porous carbon with improved electrochemical performance, Electrochim. Acta 211 (2016) 289–296, https://doi.org/10.1016/j.electacta.2016.06.055.

[44] S. Jayaraman, A. Jain, M. Ulaganathan, E. Edison, M.P. Srinivasan, R. Balasubramanian, V. Aravindan, S. Madhavi, Li-ion vs. Na-ion capacitors: a performance evaluation with coconut shell derived mesoporous carbon and natural plant based hard carbon, Chem. Eng. J. 316 (2017) 506–513, https://doi.org/10.1016/j.cej.2017.01.108.

[45] G. Wang, C. Lu, X. Zhang, B. Wan, H. Liu, M. Xia, H. Gou, G. Xin, J. Lian, Y. Zhang, Toward ultrafast lithium ion capacitors: a novel atomic layer deposition seeded preparation of $Li_4Ti_5O_{12}$/graphene anode, Nano Energy 36 (2017) 46–57, https://doi.org/10.1016/j.nanoen.2017.04.020.

[46] J. Xu, Y. Li, L. Wang, Q. Cai, Q. Li, B. Gao, X. Zhang, K. Huo, P.K. Chu, High-energy lithium-ion hybrid supercapacitors composed of hierarchical urchin-like WO_3/C anodes and MOF-derived polyhedral hollow carbon cathodes, Nanoscale 8 (2016) 16761–16768, https://doi.org/10.1039/c6nr05480c.

[47] L. Ye, Q. Liang, Y. Lei, X. Yu, C. Han, W. Shen, Z.-H. Huang, F. Kang, Q.-H. Yang, A high performance Li-ion capacitor constructed with $Li_4Ti_5O_{12}$/C hybrid and porous graphene macroform, J. Power Sources 282 (2015) 174–178, https://doi.org/10.1016/j.jpowsour.2015.02.028.

[48] C.-M. Lai, T.-L. Kao, H.-Y. Tuan, Si nanowires/Cu nanowires bilayer fabric as a lithium ion capacitor anode with excellent performance, J. Power Sources 379 (2018) 261–269, https://doi.org/10.1016/j.jpowsour.2018.01.046.

[49] E. Lim, W.-G. Lim, C. Jo, J. Chun, M.-H. Kim, K.C. Roh, J. Lee, Rational design of Li$_3$VO$_4$@carbon core–shell nanoparticles as Li-ion hybrid supercapacitor anode materials, J. Mater. Chem. A. 5 (2017) 20969–20977, https://doi.org/10.1039/C7TA05863B.

[50] Y. Gogotsi, P. Simon, True performance metrics in electrochemical energy storage, Science 334 (2011) 917–918, https://doi.org/10.1126/science.1213003.